Results in Engineering 20 (2023) 101472

Contents lists available at ScienceDirect

Results in Engineering

journal homepage: www.sciencedirect.com/journal/results-in-engineering

Predicting airfoil stalling dynamics using upwind numerical solutions to non-viscous equations

Tohid Adibi [a,**], Seyed Esmail Razavi [b], Shams Forruque Ahmed [c], Hussein Hassanpour [d], Suvash C. Saha [e], S.M. Muyeen [f,*]

[a] School of Mechanical Engineering, University of Bonab, Bonab, Iran
[b] School of Mechanical Engineering, University of Tabriz, Tabriz, Iran
[c] Science and Math Program, Asian University for Women, Chattogram, 4000, Bangladesh
[d] School of Automotive Engineering, Iran University of Science and Technology, Tehran, Iran
[e] School of Mechanical and Mechatronic Engineering, University of Technology Sydney, Ultimo, NSW, 2007, Australia
[f] Department of Electrical Engineering, Qatar University, Doha, Qatar

ARTICLE INFO

Keywords:
Dynamic stall
Airfoil
Euler equations
Vortex
Navier-Stokes
Non-viscous

ABSTRACT

Over the last few decades, researchers have been focusing on determining the critical attack angle at which dynamic stall occurs. This angle is usually determined by solving the Navier-Stokes equations, which include viscosity, pressure, gravity, and acceleration terms. However, Navier-Stokes equations are quite complex to solve and consequently difficult to simulate, thus the simulation is not accurate enough. Therefore, this article predicts the critical attack angle for the first time using Euler equations devoid of viscous terms. One of the key advantages of Euler equations is their ability to capture the vortices and predict stall dynamics. The Euler equations are thus integrated and the resulting equations are discretized using the finite volume method. A first-order upwind-based method is used to calculate the convective fluxes at the cell boundaries in the finite volume approach. A NACA 0012 airfoil is chosen for this study at various attack angles with a Mach number of 0.3. Based on the justification of Crocco's theorem, the Euler equations successfully act as Navier-Stokes equations. The vortex patterns are found to behave independently of the artificial dissipation. All the vortices are successfully predicted using the inviscid governing equations. The numerical results obtained are validated by other published experimental and numerical data.

1. Introduction

The stall of an airfoil is a rapid drop in its usual force after a rise in attack angle that results in flow separation. In other words, the dynamic stall is a nonlinear unsteady aerodynamic effect caused by vortex shedding around an airfoil. The dynamic stall was seen in helicopter manufacturing for the first time, where significant torsional fluctuations of the blades were detected. This was a thoughtful problem, restraining the velocity and mass of the helicopter. The stall would also occur on the wings of modern fighter aircraft, the blades of axial-flow compressors, and the rotors of the most efficient wind turbines [1]. There are three methods to investigate the stall phenomenon. The first method is the analytical method, which is generally inconclusive because the equations governing the flow are so complicated. The second method is the experimental method, which is less noticed by researchers due to its high costs. The third is the numerical method, which has expanded rapidly over the past few decades. Numerous researchers used numerical methods to simulate complex flows [2,3]. Numerical In recent years, there have been considerable efforts to extend the multi-dimensional numerical scheme [4–8] for solving hyperbolic equations. However, there have been many novelties in multi-dimensional schemes since the mid-1980s. These schemes have been created by computational fluid dynamics researchers to improve the numerical method. The new schemes had either better accuracy, convergence speed, or stability. Sometimes the new scheme was better in all critical aspects of computational fluid dynamics.

The normal averaging scheme was developed by Billet and Toro [9] to improve on the previous ones. The proposed scheme was used to solve

* Corresponding author.
** Corresponding author.
E-mail addresses: tohidadibi@gmail.com (T. Adibi), sm.muyeen@qu.edu.qa (S.M. Muyeen).

https://doi.org/10.1016/j.rineng.2023.101472
Received 29 April 2023; Received in revised form 12 September 2023; Accepted 22 September 2023
Available online 30 September 2023

the Euler equations numerically. The averaging schemes do not have good stability usually but the results prove that this proposed method is good enough in terms of stability and convergence speed. This method was used to solve three-dimensional fluid flow with an explosion in a finite volume framework with Cartesian grids. Fey [10] worked on Euler equations where the velocity was considered high and thus the Mack number was more than 0.3 and the density was not constant. He proposed a new three-dimensional flux-vector-splitting method that performed well at medium mack numbers. However, this method was not found good enough at sonic flows due to the lack of consistency. A multidimensional upwind scheme was proposed by Razavi et al. [11] for incompressible flows originating from a compressible-based formulation. Adibi and Razavi [12,13] extended the multidimensional characteristic method to two-dimensional flow with heat transfer. They applied their proposed scheme in flow between two parallel plates, flow within a squared cavity, and the thermos-flow over a cylinder.

The dynamic stall of thin airfoil was experimentally and numerically studied by Fan et al. [14]. The shear stress transport scheme was used for numerical simulations. Zhu et al. [15] researched the dynamic stall in three-dimensional flow over a rotating airfoil. The simulation was performed by numerical solution of time-dependent viscous three-dimensional incompressible equations. They compared the resulting outcomes with the two-dimensional one and the non-rotating airfoil results. They proposed some techniques to delay the dynamic stall, which resulted in a considerable increase in lift coefficient. Tirandaz and Rezaeiha [16] simulated an airfoil in a three-dimensional computational domain by a fourth-order averaging method. They changed the radius of the leading edge and the maximum thickness of the airfoil and repeated the numerical solutions. The simulations were carried out for different airfoils such as NACA (National Advisory Committee for Aeronautics) 0018 and NACA0024. The dynamics stall point, lift coefficient, drag coefficient, and pressure distribution of these airfoils were compared with each other, and thus the optimum design was reported. Zhao et al. [16] analyzed the flow over a two-dimensional NACA0021 numerically. The two-dimensional incompressible Navier-Stokes was solved by a large eddy numerical method. Their results revealed the dynamics of stall point, separation point, well as lift and drag forces.

Shailesh et al. [17] simulated two-dimensional flow over NACA 0012 airfoil numerically. The vortex-shedding phenomena were depicted in different conditions. Sogukpinar [18] integrated the corner transport upwind algorithm offered by Colella [19] with the wave propagation scheme of Le Veque et al. [20]. The created scheme was utilized to simulate the subsonic and sonic flows in a finite volume framework. The triangle and the cartesian grids were used in their simulations. Hadian and Yazdi [21] used Euler equations for numerical simulations of incompressible flow, which were improved by artificial compressibility. Their results showed that the Euler equation could be used for some engineering problems. Some changes were made to the flux vector splitting scheme and a novel scheme was proposed by Payganeh [22] to solve compressible flows numerically. The authors simulated the sonic and subsonic flows with their proposed scheme by the finite difference method.

Soltani et al. [23] studied the influence of the attack angle on the time-dependent subsonic and supersonic flow characteristics as a stall. In this simulation, the Navier-Stokes equations were solved numerically by a second-order finite element method. Through the literature survey, it is seen that all the research conducted on the dynamic stall has employed Navier-Stokes's equations although the Euler equations are a good alternative. Additionally, due to the complexity of Navier-Stokes equations, it is difficult to solve and hence difficult to simulate, resulting in an insufficiently accurate simulation. Therefore, the current work aims to extend a three-dimensional numerical method in a finite volume framework to solve Euler equations in the stall situation. This paper also applies the Euler equations for predicting the rotational flow pattern. In this work, an upwind scheme proposed by Ren and Sun [24] is developed and successfully employed this scheme for simulating the stall behavior.

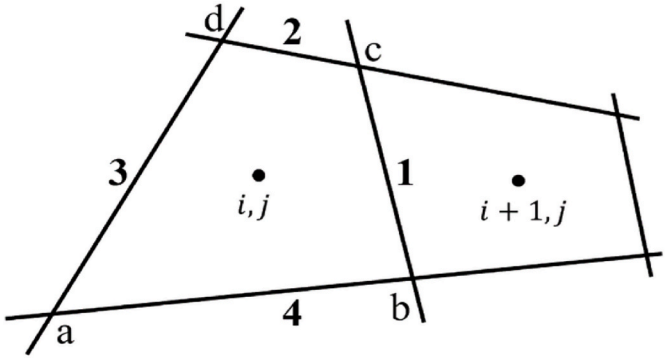

Fig. 1. Arbitrary finite-volumes.

2. Mathematical modeling and numerical schemes

Fluid flows are subject to a wide range of forces. Forces caused by pressure, gravitational force, and forces caused by shear stress are among these forces. By considering all available forces, the Navier-Stokes equations are obtained, which are very complex in nature. The first and second derivatives are included in these equations. The shear stress forces are negligible if the Reynolds number of the flow is large because the inertial forces are much greater than the viscous forces. When the shear stress in a flow is zero, the velocity gradient is also zero. The Navier-Stokes equations can be converted into the Euler equations by neglecting the shear stress forces. Since the viscous terms were eliminated, no second derivatives are present in these equations. It is thus much simpler to solve Euler's equations than Navier-Stokes equations. When it comes to studying fluid flows, Euler's equations hold a very special place. The well-known Bernoulli equation is a special case of this equation. Acceleration, Earth's gravity, and pressure are all included in Euler's equations. These formulas are written in a three-dimensional coordinate system. The two-dimensional incompressible Euler equations (inviscid equation) in the integral form are given by [25].

$$\frac{\partial}{\partial t}\iint_{\Omega} Z dx dy + \oint_{\partial\Omega} (N dy - M dx) = 0$$

$$Z = \begin{bmatrix} \rho \\ \rho u \\ \rho v \\ \rho E \end{bmatrix}, N = \begin{bmatrix} \rho u \\ \rho u^2 + p \\ \rho uv \\ \rho uH \end{bmatrix}, M = \begin{bmatrix} \rho v \\ \rho uv \\ \rho v^2 + p \\ \rho vH \end{bmatrix} \quad (1)$$

$$E = \frac{p}{(\gamma - 1)\rho} + \frac{1}{2}\left(u^2 + v^2\right), H = E + \frac{p}{\rho}$$

where γ is the specific heat ratio, u and v are the velocities in x and y-direction respectively, E is the total specific energy, ρ is the density, p is the pressure, and H is the enthalpy. The above equations have been presented in integral forms because they will be discretized by a novel upwind scheme in the finite volume framework, and it is necessary to have the equation in integral form in each cell in the computational domain. Arbitrary cells, boundaries, and remarks are shown in Fig. 1.

For each cell, Eq. (1) converts to the following form:

$$\left(\frac{\partial Z}{\partial t}\right)\varphi_{abcd} = -\sum_{k=1}^{4}(N\Delta y - M\Delta x)_k \quad (2)$$

where φ is the cell area, F_k and G_k are convective fluxes that are modeled in the following section. Now, the Euler Equations forms are changed to

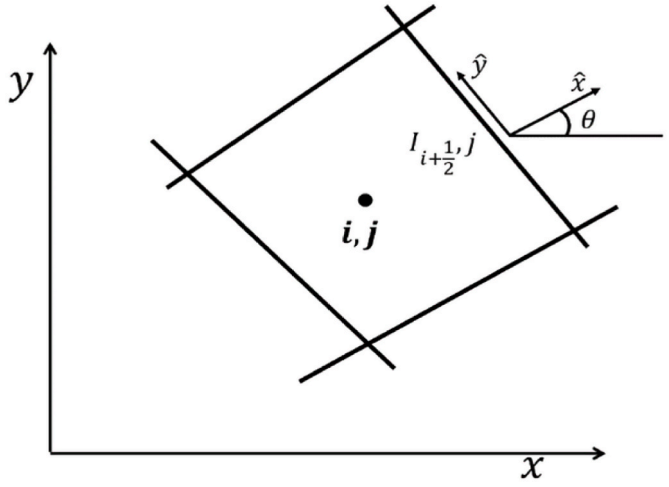

Fig. 2. Local coordinates of a cell.

be in a characteristic form. A local coordinate system $(\hat{x},\hat{y})$ is constructed where the $\hat{x}$-axis has been affiliated with $n_{i+\frac{1}{2}j}$, the external vector. It has a unit magnitude and its direction is perpendicular to the cell border which is shown in Fig. 2. The Euler equations for inviscid flow in basic variables form in the reference framework $(\hat{x},\hat{y})$ is obtained and presented in Eq. (3).

$$\frac{\partial \widehat{W}}{\partial t}+A\frac{\partial \widehat{W}}{\partial \hat{x}}+B\frac{\partial \widehat{W}}{\partial \hat{y}}=0$$

$$\widehat{W}=\begin{pmatrix}\rho\\ \hat{u}\\ \hat{v}\\ p\end{pmatrix}, P=\begin{pmatrix}\hat{u} & \rho & 0 & 0\\ 0 & \hat{u} & 0 & \frac{1}{\rho}\\ 0 & 0 & \hat{u} & 0\\ 0 & \gamma p & 0 & \hat{u}\end{pmatrix}, Q=\begin{pmatrix}\hat{v} & 0 & \rho & 0\\ 0 & \hat{v} & 0 & 0\\ 0 & 0 & \hat{v} & \frac{1}{\rho}\\ 0 & 0 & \gamma p & \hat{v}\end{pmatrix} \tag{3}$$

$$\hat{u}=v\sin\theta+u\cos\theta, \hat{v}=v\cos\theta-u\sin\theta$$

where $\hat{u}$ and $\hat{v}$ are the components of the velocity vector along the "x" and "y" direction, respectively, and θ is the angle between $n_{i+\frac{1}{2}j}$ and the x-axis, i.e.,

$$\cos\theta=\left(\frac{\Delta y}{\sqrt{(\Delta x)+(\Delta y)}}\right), \sin\theta=\left(\frac{-\Delta x}{\sqrt{(\Delta x)+(\Delta y)}}\right) \tag{4}$$

After calculating the right and left sides of the primitive variables, the following are obtained:

$$W^{R}_{i+\frac{1}{2}j}=W\left(x_{i+\frac{1}{2}j},y_{i+\frac{1}{2}j}\right)\Big|_{(x,y)\in\Omega_{i+1,j}}$$
$$W^{L}_{i+\frac{1}{2}j}=W\left(x_{i+\frac{1}{2}j},y_{i+\frac{1}{2}j}\right)\Big|_{(x,y)\in\Omega_{i,j}} \tag{5}$$

At the interface, $I_{i+\frac{1}{2}j}$, a reference state is computed by:

$$\widetilde{W}=\frac{1}{2}\left(W^{L}_{i+\frac{1}{2}j}+W^{R}_{i+\frac{1}{2}j}\right) \tag{6}$$

Eq. (6) is linearized about $\widetilde{W}$ as

$$\frac{\partial \widehat{W}}{\partial t}+\widetilde{A}\frac{\partial \widehat{W}}{\partial \hat{x}}+\widetilde{B}\frac{\partial \widehat{W}}{\partial \hat{y}}=0 \tag{7}$$

where $\widetilde{A}$ and $\widetilde{B}$ are in the $(\hat{x},\hat{y})$ coordinate system. The four eigenvalues $\widetilde{A}$ are:

$$\begin{aligned}&\xi=\widetilde{\hat{u}}-\widetilde{a}, \zeta=\widetilde{\hat{u}}+\widetilde{a}, \zeta=\widetilde{\hat{u}}\\ &\widetilde{\hat{u}}=\tilde{u}\cos\theta+\tilde{v}\sin\theta, \widetilde{\hat{v}}=-\tilde{u}\cos\theta+\tilde{v}\cos\theta,\\ &\widetilde{a}=\sqrt{\gamma\frac{\widetilde{\tilde{p}}}{\widetilde{\tilde{\rho}}}}\end{aligned} \tag{8}$$

The matrix of corresponding right eigenvectors of $\widetilde{A}$ and its inverse are calculated below

$$\widetilde{R}=\begin{bmatrix}-\frac{\widetilde{\tilde{\rho}}}{\widetilde{\tilde{a}}} & 1 & 0 & \frac{\widetilde{\tilde{\rho}}}{\widetilde{\tilde{a}}}\\ 1 & 0 & 0 & 1\\ 0 & 0 & -1 & 0\\ -\widetilde{\tilde{\rho}}\widetilde{\tilde{a}} & 0 & 0 & \widetilde{\tilde{\rho}}\widetilde{\tilde{a}}\end{bmatrix}, \widetilde{R}^{-1}=\frac{1}{2}\begin{bmatrix}0 & 1 & 0 & \frac{-1}{\widetilde{\tilde{\rho}}\widetilde{\tilde{a}}}\\ 2 & 0 & 0 & \frac{-2}{\widetilde{\tilde{a}}^{2}}\\ 0 & 0 & -2 & 0\\ 0 & 1 & 0 & \frac{1}{\widetilde{\tilde{\rho}}\widetilde{\tilde{a}}}\end{bmatrix} \tag{9}$$

Multiplying Eq. (7) by $\widetilde{R}^{-1}$,

$$\widetilde{R}^{-1}\frac{\partial \widehat{W}}{\partial t}+\widetilde{R}^{-1}\widetilde{A}\frac{\partial \widehat{W}}{\partial \hat{x}}+\widetilde{R}^{-1}\widetilde{B}\frac{\partial \widehat{W}}{\partial \hat{y}}=0 \tag{10}$$

It should be noted that since $\widetilde{R}$ does not depend on time, the following can be written

$$\frac{\partial \widetilde{R}^{-1}}{\partial t}=0, \frac{\partial \widetilde{R}^{-1}}{\partial \hat{x}}=0, \frac{\partial \widetilde{R}^{-1}}{\partial \hat{y}}=0 \tag{11}$$

If

$$\begin{aligned}&\widetilde{R}^{-1}\frac{\partial \widehat{W}}{\partial t}=\frac{\partial\left(\widetilde{R}^{-1}\widehat{W}\right)}{\partial t}=\frac{\partial \hat{w}}{\partial t},\\ &\widetilde{R}^{-1}\frac{\partial \widehat{W}}{\partial \hat{x}}=\frac{\partial\left(\widetilde{R}^{-1}\widehat{W}\right)}{\partial \hat{x}}=\frac{\partial \hat{w}}{\partial \hat{x}}\end{aligned} \tag{12}$$

By replacing (17) with (15), one gets

$$\begin{aligned}&\hat{w}_{t}+\begin{bmatrix}\widetilde{\hat{u}}-\widetilde{a} & 0 & 0 & 0\\ 0 & \widetilde{\hat{u}} & 0 & 0\\ 0 & 0 & \widetilde{\hat{u}} & 0\\ 0 & 0 & 0 & \widetilde{\hat{u}}+\widetilde{a}\end{bmatrix}\hat{w}_{x}=\hat{S}\\ &\hat{w}_{t}+\begin{bmatrix}\widetilde{\hat{u}}-\widetilde{a} & 0 & 0 & 0\\ 0 & \widetilde{\hat{u}} & 0 & 0\\ 0 & 0 & \widetilde{\hat{u}} & 0\\ 0 & 0 & 0 & \widetilde{\hat{u}}+\widetilde{a}\end{bmatrix}\hat{w}_{x}=\hat{S}\end{aligned} \tag{13}$$

$$\hat{w}=\begin{pmatrix}\hat{w}_{1}\\ \hat{w}_{2}\\ \hat{w}_{3}\\ \hat{w}_{4}\end{pmatrix}=\begin{bmatrix}\frac{1}{2}\left(-\frac{p}{\widetilde{\tilde{\rho}}\widetilde{\tilde{a}}}+u\cos\theta+v\sin\theta\right)\\ \rho-\frac{p}{\widetilde{\tilde{a}}^{2}}\\ u\sin\theta-v\cos\theta\\ \frac{1}{2}\left(+\frac{p}{\widetilde{\tilde{\rho}}\widetilde{\tilde{a}}}+u\cos\theta+v\sin\theta\right)\end{bmatrix}$$

The source term is determined as:

$$\widehat{S} = R^{-1}A_2(\widetilde{\widehat{W}})\frac{\partial \widehat{W}}{\partial \widehat{y}} = R^{-1}A_2(\widetilde{\widehat{W}})R\frac{\partial \widehat{w}}{\partial \widehat{y}}$$
$$= \begin{bmatrix} -\frac{1}{2}\widetilde{a}\frac{\partial \widehat{w}_3}{\partial \widehat{y}} - \widetilde{\widehat{v}}\frac{\partial \widehat{w}_1}{\partial \widehat{y}} \\ -\widetilde{\widehat{v}}\frac{\partial \widehat{w}_2}{\partial \widehat{y}} \\ -\widetilde{a}\frac{\partial \widehat{w}_1}{\partial \widehat{y}} + \widetilde{a}\frac{\partial \widehat{w}_4}{\partial \widehat{y}} - \widetilde{\widehat{v}}\frac{\partial \widehat{w}_3}{\partial \widehat{y}} \\ \frac{1}{2}\widetilde{a}\frac{\partial \widehat{w}_3}{\partial \widehat{y}} - \widetilde{\widehat{v}}\frac{\partial \widehat{w}_4}{\partial \widehat{y}} \end{bmatrix} \quad (14)$$

Unlike in Ref. [26], Eq. (14) is solved in a one-dimensional state, but the real flow is the three-dimensional flow. The governing equations contain the source term $\widehat{S}$ to account for three-dimensional flow effects. The benefits of this method include computational efficiency and ease of implementation of general finite volume schemes. The following relations are applied to solve Eq. (14).

$$\widehat{w}_{i+\frac{1}{2}j}^{n+1} = \widehat{w}_1 \begin{pmatrix} x_{i+1/2,j} - \lambda_l(n_x)^n\Delta t, \\ y_{i+1/2,j} - \lambda_l(n_y)^n\Delta t, \\ t^n \end{pmatrix} + \widehat{s}_l\Delta t, (l = 1,2,3,4) \quad (15)$$

All variations in time "n" are known and the unknown variations are obtained by using Eq. (15). All variations are known at n = 1 from initial conditions.

$$(\widehat{w}_l)_{i+1/2,j}^{n+1} = \frac{1+sign(\lambda_l)}{2}$$
$$\left\{(\widehat{w}_l)_{i,j}^n + \left(\frac{\partial w_l}{\partial x}\right)_{i,j}^n \begin{bmatrix} x_{i+1/2,j} - x_{i,j} - \\ \lambda_l(n_x)_{i+1/2,j}^n\Delta t \end{bmatrix} + \right.$$
$$\left.\left(\frac{\partial w_l}{\partial y}\right)_{i,j}^n \left[y_{i+1/2,j} - y_{i,j} - \lambda_l(n_y)_{i+1/2,j}^n\Delta t\right] + (\widehat{s}_l)_{i,j}^n\Delta t\right\} + \frac{1-sign(\lambda_l)}{2} \quad (16)$$
$$\left\{(\widehat{w}_l)_{i+1,j}^n + \left(\frac{\partial w_l}{\partial x}\right)_{i+1,j}^n \begin{bmatrix} x_{i+1/2,j} - x_{i+1,j} - \\ \lambda_l(n_x)_{i+1/2,j}^n\Delta t \end{bmatrix} + \right.$$
$$\left.\left(\frac{\partial w_l}{\partial y}\right)_{i+1,j}^n \left[y_{i+1/2,j} - y_{i+1,j} - \lambda_l(n_y)_{i+1/2,j}^n\Delta t\right] + (\widehat{s}_l)_{i+1,j}^n\Delta t\right\}$$

After determining, primitive variables are computed as

$$\widehat{W}_1 = \rho = -\frac{\widetilde{\rho}}{\widetilde{a}}\widehat{w}_1 + \widehat{w}_2 + \frac{\widetilde{\rho}}{\widetilde{a}}\widehat{w}_4, \widehat{W}_2 = \widehat{u} = \widehat{w}_1 + \widehat{w}_4,$$
$$\widehat{W}_3 = \widehat{v} = -\widehat{w}_3, \widehat{W}_4 = p = -\widetilde{\rho}\widetilde{a}\widehat{w}_1 + \widetilde{\rho}\widetilde{a}\widehat{w}_4$$
$$u = \frac{\widehat{u}\Delta y + \widehat{v}\Delta x}{\sqrt{(\Delta x)^2 + (\Delta y)^2}}, v = \frac{\widehat{v}\Delta y - \widehat{u}\Delta x}{\sqrt{(\Delta x)^2 + (\Delta y)^2}} \quad (17)$$
$$u = \frac{\widehat{u}\Delta y + \widehat{v}\Delta x}{\sqrt{(\Delta x)^2 + (\Delta y)^2}}, v = \frac{\widehat{v}\Delta y - \widehat{u}\Delta x}{\sqrt{(\Delta x)^2 + (\Delta y)^2}}$$

After obtaining ρ, u, v, p [27], the convective fluxes are calculated at the cell borders as follows:

$$F_{i+\frac{1}{2}j} = \begin{bmatrix} \rho \\ \rho u^2 + p \\ \rho vu \\ (\rho E + p)u \end{bmatrix}_{i+\frac{1}{2}j}, G_{i+\frac{1}{2}j} = \begin{bmatrix} \rho \\ \rho vu \\ \rho v^2 + p \\ (\rho E + p)v \end{bmatrix}_{i+\frac{1}{2}j} \quad (18)$$

To keep the scheme stable, it is necessary to incorporate artificial dissipation as:

$$\left(\frac{\partial U}{\partial t}\right)\Omega_{abcd} = -\sum_{k=1}^{4}(F_k\Delta y_k - G_k\Delta x_k) + DU \quad (19)$$

In this study, the effectiveness of Euler's equations in simulating stalling flows has been investigated. For the numerical method's stability, artificial dissipation terms have been employed. By using Euler's equations rather than Navier-Stokes' equations, the second-order derivatives have been omitted. The numerical solution, however, now includes another type of second-order derivatives in the form of artificial dissipation terms. These terms may have improved the results of Euler's equations by reducing the difference between the Navier-Stokes equations and Euler's equations. In this research, however, the actual viscosity of the fluid is not used as the coefficient of second-order derivatives; rather, a damping coefficient is used. Wide numerical experiments have shown that a reasonable sentence for *DU* is a combination of second and fourth-order terms [28], which functions the local pressure gradient. For the density one has:

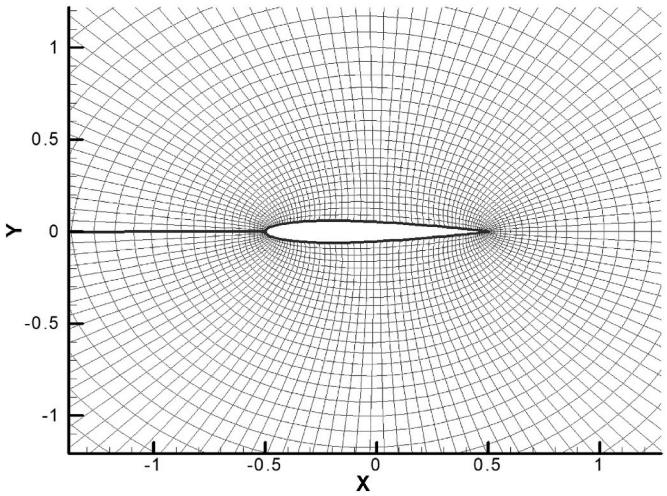

Fig. 3. A part of the O-shape grid for NACA0012, 130 × 70 cells.

$$D\rho = D_x\rho + D_y\rho \quad (20)$$

$$D_x\rho = d_{i+\frac{1}{2}j} - d_{i-\frac{1}{2}j} \quad (21)$$

with

$$d_{i+\frac{1}{2}j} = \frac{\Omega_{i,j}}{\Delta t}\begin{bmatrix} \xi_{i+\frac{1}{2}j}^{(2)}(\rho_{i+1,j} - \rho_{i,j}) \\ -\xi_{i+\frac{1}{2}j}^{(4)}(\rho_{i+2,j} - 3\rho_{i+1,j} + 3\rho_{i,j} - \rho_{i-1,j}) \end{bmatrix} \quad (22)$$

where Ω is the cell volume and the coefficients $\xi_{i+\frac{1}{2}j}^{(2)}$ and $\xi_{i+\frac{1}{2}j}^{(4)}$ have been modified to the fluid flow and defined as

$$\upsilon_{i,j} = \frac{|p_{i+1,j} - 2p_{i,j} + p_{i-1,j}|}{|p_{i+1,j}| + 2|p_{i,j}| + |p_{i-1,j}|}$$
$$\xi_{i+\frac{1}{2}j}^{(2)} = k^{(2)}\,Max(\upsilon_{i+1,j}, \upsilon_{i,j}),$$
$$\xi_{i+\frac{1}{2}j}^{(4)} = Max\left(0, k^{(4)} - \xi_{i+\frac{1}{2}}^{(2)}\right) \quad (23)$$
$$k^{(2)} = \frac{1}{4}, k^{(4)} = \frac{1}{400}$$

At the solid borders, the no-slip boundary condition has been applied, and the components of velocity are taken as zero. The local characteristics were used on the far-field boundary depending on the boundary to be either inlet or outlet. For the inlet far-field, the velocity components were considered V_{0x} and V_{0y}, and for the outlet far-field, the pressure was considered zero. The fifth-order Runge-Kutta time marching method has been used to find the variations at the new time [12]. This type (fifth-order) of the Runge-Kutta scheme is better than

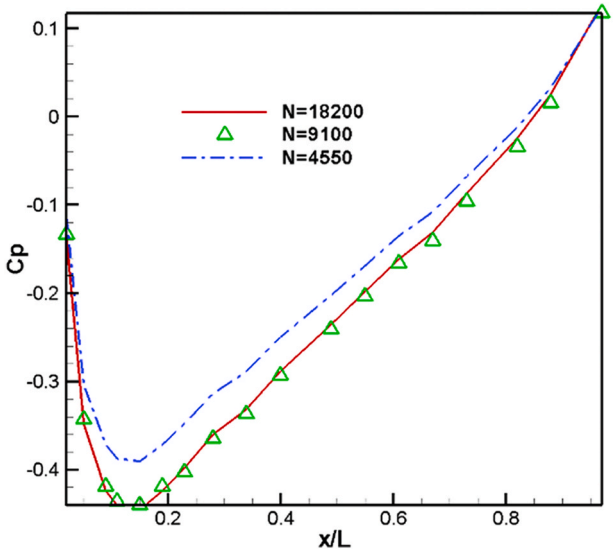

Fig. 4. Pressure coefficient variation on the external boundary of the airfoil for different numbers of grids.

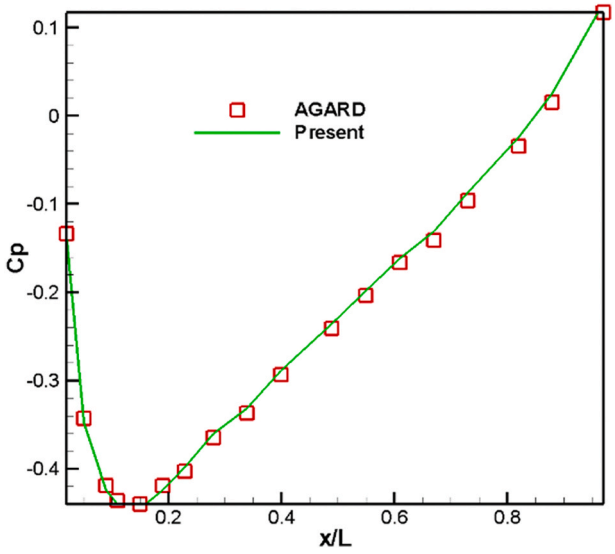

Fig. 5. Comparison of C_p at $\alpha = -0.02^{\circ}$ and $M_\infty = 0.3$ with experimental data [30].

other Runge-Kutta schemes because less memory is used in this method. Also, it is more accurate and stable than others; thus, a more extensive time step can be used, and convergence is reached sooner.

3. Numerical results

An O-grid is generated to solve the Euler equations around the airfoil, as shown in Fig. 3. The simulation of the NACA 0012 airfoil at a Mach number of 0.3 is widely recognized as a renowned benchmark. This airfoil is one of the most commonly used airfoils and is relatively thin. A general investigation was conducted in this study considering a Mach number of 0.3. A grid independence study was carried out, and the grid with 130 × 70 cells was chosen to run the simulation, where 130 is the number of cells around the airfoil, and 70 is the number of cells along the radius. The pressure coefficient on the airfoil for different mesh sizes is shown in Fig. 4. The gradient of the velocity components and the pressure is large near the solid borders, so the clustering is performed near the solid boundary for sufficient accuracy [29]. To avoid the far-field boundary effect on the flow pattern, the far-field boundary is 30 chords away from the airfoil center. To validate the numerical results of the current study, comparisons were done with the experimental data for the steady flow with $\alpha = -0.02^{\circ}$ and $M_\infty = 0.3$. As illustrated in Fig. 5, the results of the recommended numerical scheme are in good agreement with the experimental results reported by Agard [30].

The results obtained by Murthy [31] at great angles of attack, $\alpha = 30^{\circ}, 53^{\circ}$ and $M_\infty = 0.3$ are used to compare stall dynamics with other works. However, Murthy did not consider Euler's equations as he obtained his results by solving Navier-Stokes's equations. He used a third-order Roe algorithm for convective terms and a second-order averaging method for the viscous terms. Figs. 6 and 7 confirm that the present work agrees well with the results of Murthy on the creation of vortices.

According to Crocco's theorem, the main factor in vortex production is the dissipation terms [32]. For inspection of the effect of k_2 and k_4 on the vortex patterns, several numerical tests were conducted. The following was found:

a) Lowering these coefficients leads to a reduction in numerical stability.
b) A reduction in k_2 and k_4 postpones the rate of generation and growth of vortices.
c) The vortex patterns are entirely independent of these coefficients. It should be noted that Fig. 8 proves item (c).

The flow over an airfoil becomes inherently unsteady at high angles of attack. The process of vortices includes the creation, growth, and separation of states. As the angle of attack increases, the formation of trailing edge vortices begins, and the separation point moves towards

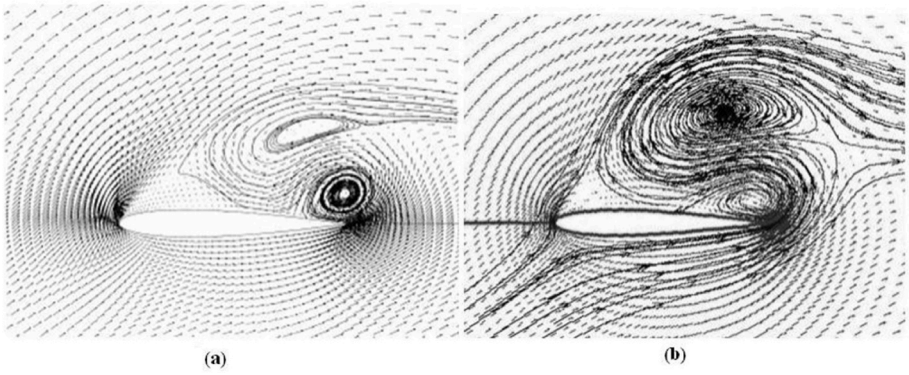

Fig. 6. Velocity vectors and streamlines around NACA-0012 airfoil, $= 30^{\circ}$, $M_\infty = 0.3$
(a) Ref [31] (b) current study results.

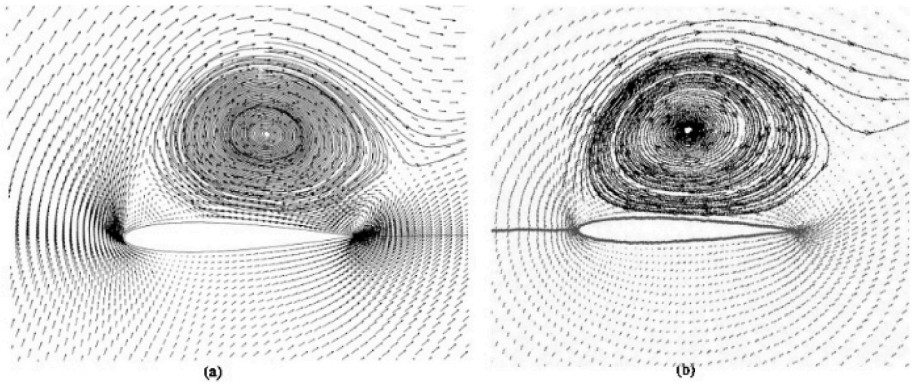

Fig. 7. Velocity vectors and streamlines around NACA 0012 airfoil, $= 53^{\circ}$, $M_{\infty} = 0.3$
(a) Ref [31] (b) current study results.

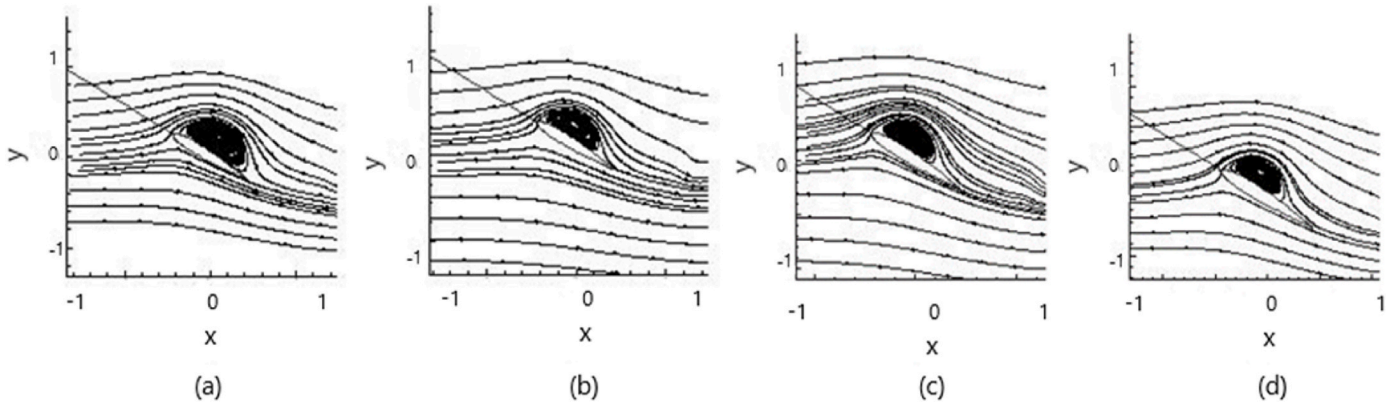

Fig. 8. Independence of vortex patterns from the dissipation coefficients of the same iteration step, $= 30^{\circ}$, $M_{\infty} = 0.3$, a) $k_2 = \frac{1}{4}, k_4 = \frac{1}{400}$, b) $k_2 = \frac{1}{7}, k_4 = \frac{1}{600}$ c) $k_2 = \frac{1}{10}, k_4 = \frac{1}{800}$ d) $k_2 = \frac{1}{20}, k_4 = \frac{1}{1000}$.

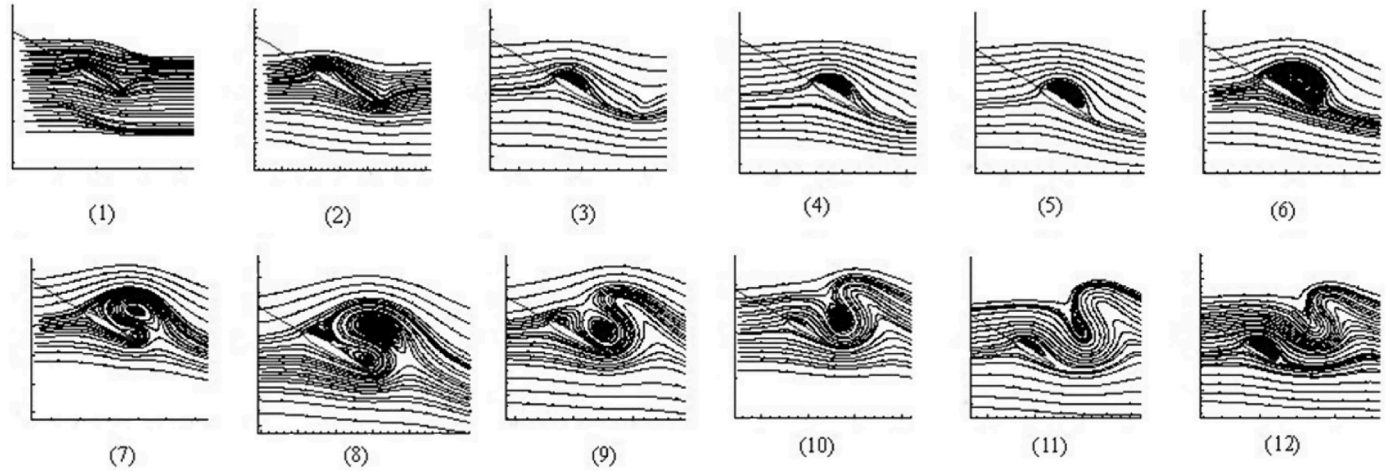

Fig. 9. The evolution of unsteady streamlines and vortices around NACA-0012 airfoil, $\alpha = 30^{\circ}$, $M_{\infty} = 0.3$.

the leading edge, generating a sheer layer whose origin follows the separation point. Therefore, the shear layer instability rollers also follow the kinematics of the separation point. The separation line has approached the leading-edge region forming a final shear layer at the end of this process. The dynamic stall vortex is formed when the instability rollers of this shear layer eventually pair. When the above process takes place, the trailing edge stops shedding vortices because of total vorticity conservation. It is noted that this vortex rotates clockwise (CW). This pattern occurs periodically, which has been depicted in Figs. 9 and 10.

At greater attack angles, the lift coefficient is affected by the formation, growth, and separation of vortices. Regarding this phenomenon, the followings are observed:

a) The leading-edge vortices, which rotate clockwise, increase the lift coefficient.

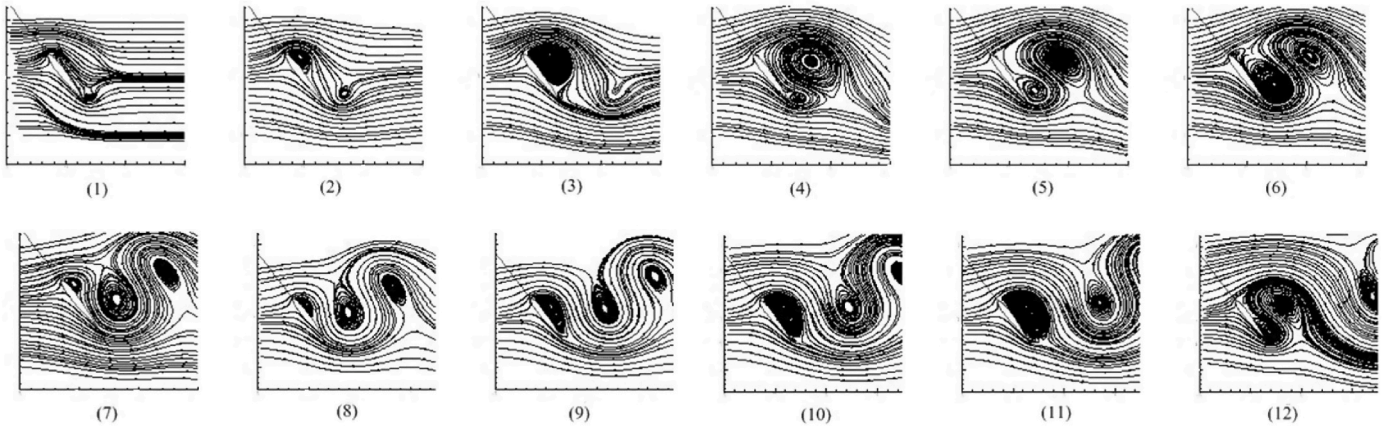

Fig. 10. The evolution of unsteady streamlines and vortices around NACA-0012 airfoil, $\alpha = 53^{\circ}$, $M_{\infty} = 0.3$.

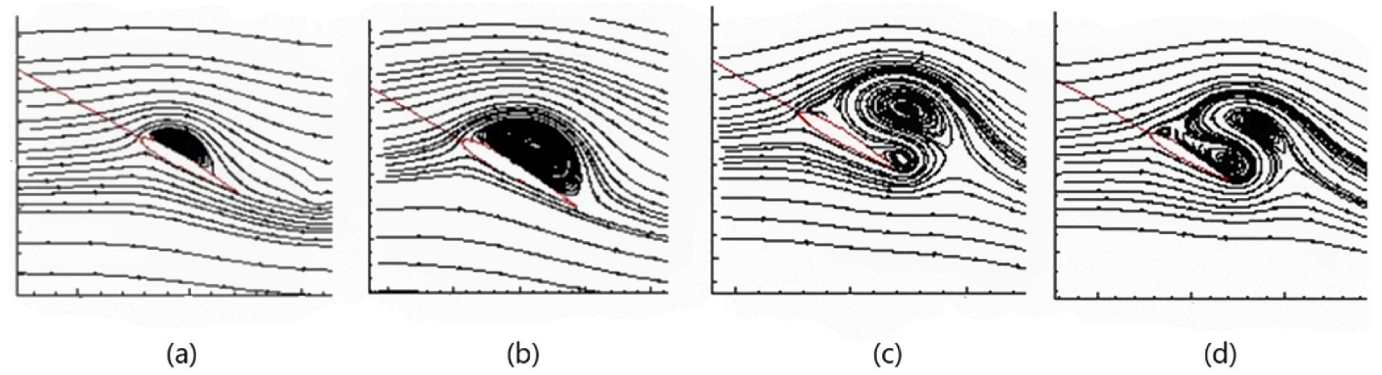

Fig. 11. The process of unsteady streamlines and corresponding lift coefficients around NACA-0012 airfoil, $= 30^{\circ}$, $M_{\infty} = 0.3$, a) $C_L = 2.3$, b) $C_L = 3.2$, c) $C_L = 1.6$, d) $C_L = 0.12$.

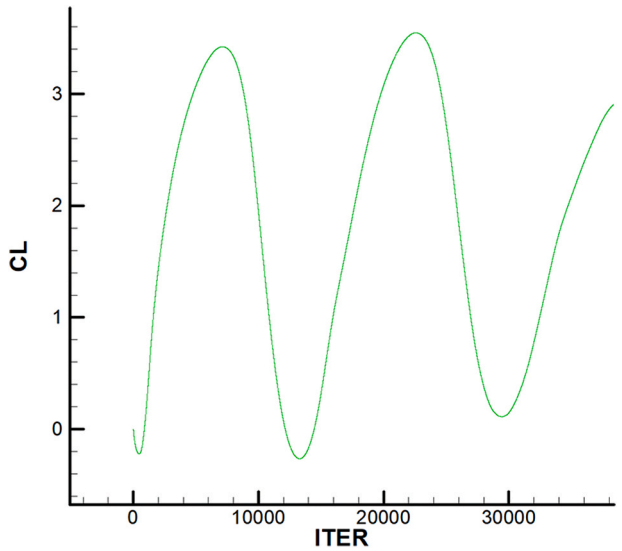

Fig. 12. The variation of lift coefficient in the time at $= 30^{\circ}$, $M_{\infty} = 0.3$.

b) The trailing edge vortices rotate counterclockwise, and the separation of vortices decreases the lift coefficient.

The details are shown in Fig. 11. The time variation of the lift coefficient at a relatively high angle of attack is illustrated in Fig. 12. As seen in the figure, this variation is periodic.

It is important to point out that while the simulations performed using Euler's equations produced very satisfactory results, the use of these equations will have severe limitations in some flows. Low Reynolds number flows, where viscous forces are comparable to or greater than inertial and gravity forces, are concluded by these Flows. Large errors are introduced into the calculations when the shear stress is ignored and the second derivatives are omitted in these flows. Therefore, the aforementioned constraints should be taken into account when employing Euler's equations. New work can be done in the same vein as future work. Using Euler's equations, researchers can model the flow around different airfoils and compare the simulated results to those obtained from experiments. Flow simulations around complex geometries, such as a cylinder, are also of interest to scientists.

4. Conclusion

An explicit upwind-based flux treatment was developed in the present study for solving the Euler equations. Certain mathematical operations were performed on the governing equations to determine the characteristics of the flow in order to obtain the new scheme. Some mathematical operations were applied to the governing equations to determine the flow characteristics, resulting in the new scheme. An upstream method was then established based on the obtained characteristics. The newly developed scheme was applied to Euler's equations. As an incompressible flow solver, Euler equations were used to capture flow details such as the vortex generation and shedding process. Crocco's theorem also supported this finding. Another aspect of this research was the use of a time-marching approach to record the vortex formation, shedding, and separation scenarios. Fourth-order Runge-Kutta method

was used for time marching.

The results demonstrates that artificial dissipation has no effect on the viscous flow behavior of inviscid time-marching solvers. It is also found that the Euler equation is comparable to the Navier-Stokes equations in capturing flow details such as dynamic stall. At greater attack angles, the formation, growth, and separation of vortices influence the lift coefficient. The vortices at the leading edge, which rotate clockwise, increase the lift coefficient. Vortices at the trailing edge rotate counterclockwise, and their separation reduces the lift coefficient. Since the outcomes of this study are useful for numerical simulations, it is applicable to various industries, such as aircraft and automobile manufacturing. The proposed scheme could be utilized in the future for additional case studies involving various airfoils. Furthermore, it could be used to simulate supersonic flows. However, more research and development are needed to fully exploit the potential of the proposed property of Euler equations.

Declaration of competing interest

The authors declare that they have no known competing financial interests or personal relationships that could have appeared to influence the work reported in this paper.

Data availability

No data was used for the research described in the article.

Acknowledgment

Open Access funding provided by the Qatar National Library.

References

[1] C.J. Ejeh, G.P. Akhabue, E.A. Boah, K.K. Tandoh, Evaluating the influence of unsteady air density on the aerodynamic performance of a fixed-wing aircraft at different angle of attack using computational fluid dynamics, Results Eng. 4 (2019) 100037.
[2] J. Alqallaf, J.A. Teixeira, Numerical study of effects of solid particle erosion on compressor and engine performance, Results Eng. 15 (2022) 100462.
[3] S.M. Fakhari, M. Ben Hassen, H. Mrad, Optimizing the operation safety and performance of an axial compressor using fluid-structure coupling and high-performance computing, Results Eng. 18 (2023) 101061.
[4] A. Khalid, et al., Numerical approximation for the solution of linear sixth order boundary value problems by cubic B-spline, Adv. Differ. Equ. 2019 (1) (2019) 1–16.
[5] A.A. El-Sayed, P. Agarwal, Numerical solution of multiterm variable-order fractional differential equations via shifted Legendre polynomials, Math. Methods Appl. Sci. 42 (11) (2019) 3978–3991.
[6] A. El-Sayed, D. Baleanu, P. Agarwal, A novel Jacobi operational matrix for numerical solution of multi-term variable-order fractional differential equations, J. Taibah Univ. Sci. 14 (1) (2020) 963–974.
[7] S. Kumar, et al., An optimal fourth order derivative-free numerical algorithm for multiple roots, Symmetry 12 (6) (2020) 1038.
[8] P. Agarwal, R. Singh, A. ul Rehman, Numerical solution of hybrid mathematical model of dengue transmission with relapse and memory via Ada–Bashforth–Moulton predictor-corrector scheme, Chaos, Solit. Fractals 143 (2021) 110564.
[9] S.J. Billett, E.F. Toro, Unsplit WAF-type schemes for three dimensional hyperbolic conservation laws, in: E.F. Toro, J.F. Clarke (Eds.), Numerical Methods for Wave Propagation: Selected Contributions from the Workshop Held in Manchester, U.K., Containing the Harten Memorial Lecture, Springer Netherlands, Dordrecht, 1998, pp. 75–124.
[10] M. Fey, Multidimensional upwinding. Part II. Decomposition of the euler equations into advection equations, J. Comput. Phys. 143 (1) (1998) 181–199.
[11] K. Zamzamian, S.E. Razavi, Multidimensional upwinding for incompressible flows based on characteristics, J. Comput. Phys. 227 (19) (2008) 8699–8713.
[12] T. Adibi, S.E. Razavi, A new characteristic approach for incompressible thermo-flow in Cartesian and non-Cartesian grids, Int. J. Numer. Methods Fluid. 79 (8) (2015) 371–393.
[13] S.E. Razavi, T. Adibi, A novel multidimensional characteristic modeling of incompressible convective heat transfer, J. Appl. Fluid Mech. 9 (4) (2016) 1135–1146.
[14] C. Fan, Y. Wu, Y. Yu, A. Wang, Dynamic thin-airfoil stall and leading-edge stall of oscillating wings at low Reynolds number, Fluid Dynam. 54 (5) (2019) 691–704.
[15] C. Zhu, Y. Qiu, T. Wang, Dynamic stall of the wind turbine airfoil and blade undergoing pitch oscillations: a comparative study, Energy 222 (2021) 120004.
[16] M.R. Tirandaz, A. Rezaeiha, Effect of airfoil shape on power performance of vertical axis wind turbines in dynamic stall: symmetric Airfoils, Renew. Energy 173 (2021) 422–441.
[17] S.K. Jha, et al., Investigations of flow phenomena over a flat plate and NACA0012 airfoil at high angles of attack, Iran. J. Sci. Technol., Transact. Mech. Eng. 40 (2020) 985–996.
[18] H. Sogukpinar, Numerical investigation of influence of diverse winglet configuration on induced drag, Iran. J. Sci. Technol. Transact. Mech. Eng. 44 (1) (2020) 203–215.
[19] P. Colella, Multidimensional upwind methods for hyperbolic conservation laws, J. Comput. Phys. 87 (1) (1990) 171–200.
[20] R.J. LeVeque, Wave propagation algorithms for multidimensional hyperbolic systems, J. Comput. Phys. 131 (2) (1997) 327–353.
[21] A. Hadian, S.R. Sabbagh Yazdi, Pressure-velocity coupled finite volume solution of steady incompressible invscid flow using artificial compressibility technique, Int. J. Eng. 17 (2) (2004) 109–118.
[22] G. Payganeh, A. Hadidi, M. Hallaji, N. Garjasi, The numerical simulation of compressible flow in a Shubin nozzle using schemes of Bean-Warming and flux vector splitting, J. Comput. Appl. Res. Mech. Eng. 1 (2) (2012) 111–118.
[23] M.R. Dr Soltani, Effect of amplitude and mean angle of attack on the unsteady surface pressure of a pitching airfoil, J. Aero. Sci. Technol. 2 (4) (2005) 9–26.
[24] Y.-X. Ren, Y. Sun, A multi-dimensional upwind scheme for solving Euler and Navier–Stokes equations, J. Comput. Phys. 219 (1) (2006) 391–403.
[25] sajjadi, h., S.F. Hosseinizadeh, and Y. Vazifehshenas, Verification of a CFD solver in near ground effect for aerodynamic behavior of airfoil NACA 0015, J. Aero. Sci. Technol. 8 (1) (2011) 1–10.
[26] M. Brio, A.R. Zakharian, G.M. Webb, Two-dimensional riemann solver for euler equations of gas dynamics, J. Comput. Phys. 167 (1) (2001) 177–195.
[27] ibrahim, s.M. K. Suneetha, G.V.R. Reddy, A study on free convective heat and mass transfer flow through a highly porous medium with radiation, chemical reaction and Soret effects, J. Comput. Appl. Res. Mech. Eng. 8 (2) (2019) 121–132.
[28] X. Liu, et al., Improved dynamic stall prediction of wind turbine airfoils, Energy Proc. 158 (2019) 1021–1026.
[29] A. Khalkhali, H. Safikhani, Applying evolutionary optimization on the airfoil design, J. Comput. Appl. Res. Mech. Eng. 2 (1) (2012) 51–62.
[30] AGARD. Experimental Data Base for Computer Program Assessment; report of the fluid dynamics panel, 1979. AGARD Advisory.
[31] P.S. Murthy, V.S. Holla, H. Kamath, Unsteady Navier–Stokes solutions for a NACA 0012 airfoil, Comput. Methods Appl. Mech. Eng. 186 (1) (2000) 85–99.
[32] M.R. Petritchenko, Rough estimates and binomial approximations for Crocco's equation in the boundary problems, St. Petersburg Polytech. Univ. J.: Phys. Math. 1 (4) (2015) 381–391.